Lab on a Chip

ROYAL SOCIETY OF CHEMISTRY

PAPER

View Article Online
View Journal

Cite this: DOI: 10.1039/d5lc01171j

A 3D microfluidic model of exchange between perfused blood and lymphatic microvascular networks

Delaney Gray-Scherr, [ab] Terry Ching, [ab] Katherine Beran, [a] Sarah C. Adams, [a] Emily Davis, [ab] Abraham C. I. van Steen, [ab] Trisha Raman, [a] Wilson W. Wong, [a] Jeroen Eyckmans [ab] and Christopher S. Chen *[ab]

Blood and lymphatic microvascular networks function as integrated systems within tissues, exchanging fluid, molecules, and cells to regulate homeostasis and immune responses, yet current *in vitro* models primarily study these systems in isolation. Existing blood-lymphatic culture models either lack *in vivo*-like network architecture or cannot achieve independent perfusion of the two vascular compartments, preventing their use in modeling cross-network transport interactions. Here, we present a novel microfluidic platform that supports the formation of independently perfusable, self-assembled blood and lymphatic microvascular networks with physiologically relevant architecture, surface area, and spatial organization. This model was created using a tape-based laminated microfluidic device and sequential gel casting approach to spatially pattern blood and lymphatic endothelial cells within a continuous matrix environment, allowing the two networks to co-develop and become independently perfusable without compromising cross-network transport capacity. High-resolution imaging confirmed that both networks matured progressively over 5 days, maintaining distinct identities, morphology, and barrier integrity under optimized growth factor conditions. Functional validation demonstrated size-selective transport between networks and physiologically relevant T-cell migration from blood to lymphatic vessels, with enhanced trafficking under inflammatory (TNF-α), chemoattractant (SDF-1α), and activation conditions. These studies establish a new experimental platform for the investigation of molecular and cellular transport and signaling across the blood-lymphatic interface under diverse physiological and pathological conditions.

Received 19th December 2025,
Accepted 25th March 2026

DOI: 10.1039/d5lc01171j

rsc.li/loc

Introduction

Blood and lymphatic microvascular networks serve as fundamental regulators of tissue homeostasis and immunity, mediating the coordinated transport of fluid, molecules, and immune cells throughout the body.[1–3] Disruption of this coordinated transport drives numerous disease processes including cancer metastasis, chronic inflammation, and lymphedema.[1,4,5] Yet despite this critical importance, the mechanisms governing the complex interplay between these networks remain poorly understood—a knowledge gap partially attributable to difficulties in studying these interactions *in vivo* in addition to limitations in current *in vitro* models.[6,7]

Microfluidic technology has enabled detailed analysis of blood vessel formation, function, and barrier properties in controlled 3D environments,[8–11] while lymphatic microfluidic models have more recently emerged to study lymphangiogenesis and lymphatic barrier function.[7,12–15] However, this compartmentalized approach—where blood and lymphatic networks are developed in separate devices—fundamentally limits investigation of their cross-talk, a critical interaction that is essential for understanding tissue homeostasis and disease progression.

Current blood–lymphatic co-culture approaches fall into two main categories, each with distinct strengths and limitations. Barrier models—including 2D membrane systems and simplified 3D endothelium-lined channels[16–18]—excel in permeability assays,[16,18] detailed analysis of endothelial junctions,[16] and immune and cancer cell transmigration across set interfaces,[17] but typically lack the *in vivo*-like network architecture, extended surface area, and spatial complexity of microvascular beds where cross-network transport occurs at tissue scale. In contrast, 3D network

[a] *Department of Biomedical Engineering and the Biological Design Center, Boston University, Boston, MA 02215, USA. E-mail: chencs@bu.edu*
[b] *The Wyss Institute for Biologically Inspired Engineering at Harvard University, Boston, MA 02115, USA*

models[19–26]—including self-assembled or angiogenic microvessel systems—can generate physiologically relevant blood and lymphatic microvascular architectures and, in some cases, *in vivo* – like blood – lymphatic microvascular proximity, but to date have not combined dense, *in vivo* – scale blood and lymphatic microvascular networks with fully independent fluidic access to both compartments in a single platform designed for controlled studies of fluid, solute, and immune-cell transport between the two networks.

Here we present a novel microfluidic platform combining physiologically relevant human dermal microvascular blood (hDMVEC, hereafter 'BEC') and lymphatic (hDMLEC, hereafter 'LEC') networks with independent perfusion of both vascular compartments. Our sequential gel casting approach into a tape-based microfluidic device enables controlled compartmentalization and independent network development while maintaining network proximity essential for physiological crosstalk. Using this approach, we demonstrate formation of adjacent, independently perfusable blood and lymphatic networks with physiologically relevant surface area and spatial organization. We validate the platform's capability to model size-selective cross-network transport and T cell trafficking from blood to lymphatic circulation, demonstrating physiologically relevant functionality and providing a foundational platform for quantitative investigation of blood-lymphatic interactions in controlled *in vitro* settings.

Results

Tape-based microfluidic platform enables sequential casting of spatially adjacent blood and lymphatic microvascular networks

To co-culture blood and lymphatic microvascular networks that were spatially adjacent but fluidically independently perfusable, we developed a tape-based microfluidic platform (Fig. 1A–C and S1). The device architecture enables precise spatial patterning and controlled deposition of cell-containing fibrin solutions into distinct gel regions that link to external media reservoirs *via* larger "parent" channels.

Two critical design features enable the formation of independent perfusable networks. First, the device shape and

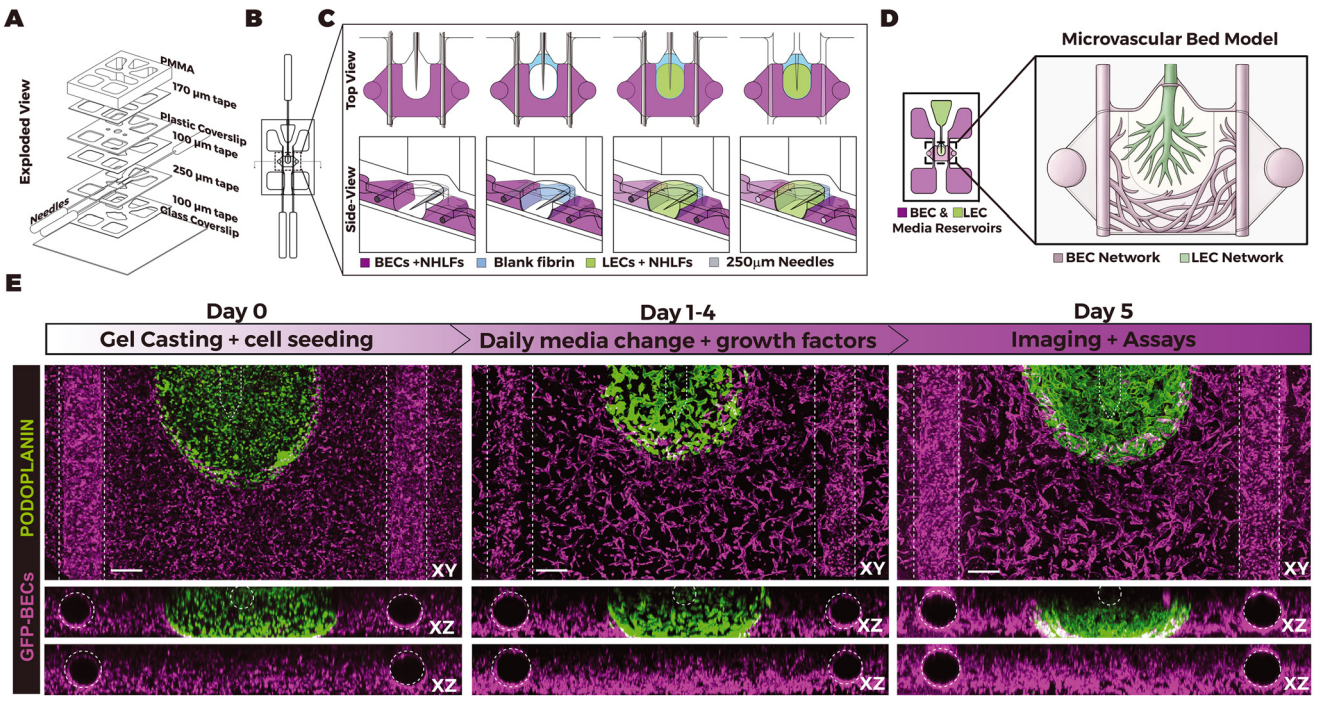

Fig. 1 Design and assembly of a microfluidic platform supporting independently perfusable blood and lymphatic microvascular networks. (A) Exploded schematic of the multi-layer, tape-based microfluidic assembly. (B) Top-down diagram of the device during gel casting, showing the placement of 250 μm needles used to mold parent channels linking media reservoirs to microvascular networks. (C) Expanded schematic of the sequential casting process used to establish spatially sequestered but functionally adjacent microvascular compartments. Endothelial cells and fibroblasts are suspended in fibrin and cast into separate regions to form a blood compartment (BECs + NHLFs, magenta) and a lymphatic compartment (LECs + NHLFs, green), separated by a thin acellular fibrin interface (blue). (D) Top-down view of the complete chip showing the casted gel regions and corresponding media reservoirs. Inset: conceptual diagram of the microvascular interface, depicting the formation of "circulatory" blood microvasculature (magenta) and blind-ended lymphatic microvasculature (green) extending from their respective parent channels. (E) Culture timeline and representative confocal images of microvascular morphogenesis. Devices were cultured for 5 days on a rocker with daily media changes of EGM2-MV supplemented with VEGFA (25 ng mL^{-1}), VEGFC (1 ng mL^{-1}), S1P (500 nM), and bFGF (25 ng mL^{-1}). Images show the self-assembly of GFP-BEC networks (magenta, anti-GFP) and LEC networks (green, anti-podoplanin) at days 1, 3, and 5. Dashed lines indicate the position and cross-section of the perfusable parent channels defined by needle removal. Scale bar: 300 μm.

material composition, together with uniform internal surface hydrophilicity achieved by functionalization, permit precise and controlled deposition of gel solutions only within designated regions (Fig. 1A–B). First, device geometry—specifically the semicircular access port in the top coverslip—and uniform internal hydrophilicity work together to form a surface-tension–based constraint that confines slowly dispensed gels to their intended compartment without spillover into the adjacent vascular compartment (Fig. 1A–B)—an approach conceptually related to earlier geometric and surface-tension-based patterning strategies.[9,27–29] Second, acupuncture needles positioned through integrated needle guides within each gel compartment sacrificially mold perfusable parent channel lumens that link the interior gel regions to external media reservoirs (Fig. 1C). This needle-casting approach allows endothelial cells seeded within the gel to eventually colonize and connect to these parent channels during vasculogenesis, establishing perfusion links to the outside of the device, as has been previously reported.[30]

During assembly, fibrin gel containing BECs and fibroblasts (NHLFs) was cast into the "blood" compartment around an inserted acupuncture needle. After partial gelation, a fibrin "wash" layer lacking thrombin was applied to the "lymphatic" cavity, creating minimal separation between the blood and lymphatic compartments while preserving a continuous matrix for molecular exchange. The lymphatic compartment was then filled with fibrin containing LECs and fibroblasts around a second acupuncture needle. Following complete polymerization, all needles were removed, and devices were sealed. Additional BECs were then introduced into the blood parent channels to coat the channel walls and promote anastomosis between the nascent microvascular network and the parent channels. Cultures were maintained on a rocker to promote flow with daily media changes containing EGM2MV supplemented with an angiogenic growth factor cocktail for 5 days.

The resulting device architecture (Fig. 1D) achieves physiologically relevant organization: the lymphatic endothelial network connects to a single parent channel linked to one media reservoir, creating unidirectional dead-ended vasculature that mimics *in vivo* lymphatic microvascular organization. In contrast, the blood endothelial network connects to two parent channels positioned at opposite ends of the device, with these channels linked to four separate media reservoirs, enabling control over circulatory flow patterns. Both networks remain in spatial proximity with a continuous matrix permitting molecular exchange.

Both networks self-assembled over 5 days with daily media changes. Confocal images (Fig. 1E) show cell organization on day 1, nascent networks extending from parent channels on day 3, and mature, interconnected networks throughout both compartments by day 5. This reproducible progression established day 5 as the standard timepoint for all subsequent analyses.

Engineered blood and lymphatic microvascular networks retain identity and display physiologically relevant architecture

By day 5, the platform generated two spatially restricted microvascular networks that remained confined to their designated gel compartments, with GFP-labeled BEC vessels and podoplanin-positive LEC vessels forming adjacent but non-overlapping networks (Fig. 2A and B and S2A and B). Immunofluorescent staining of fixed samples confirmed that LECs expressed a lymphatic phenotype ($CD31^+$/$podoplanin^+$/$Prox1^+$), whereas BECs (GFP^+) remained $CD31^+$/$podoplanin^-$/$Prox1^-$ in both 3D networks and parallel 2D monolayer cultures, indicating that co-culture and shared media did not drive detectable phenotypic convergence (Fig. S3).

VE-cadherin staining revealed continuous adherens junctions along both parent channels and connected microvessels, consistent with intact vessel integrity across the blood and lymphatic networks from the parent channels down to the microvasculature (Fig. 2C and D and S4A and B). Junctional organization differed between vessel types: BEC microvessels exhibited brighter, thicker, and more linear VE-cadherin staining, whereas lymphatic capillaries displayed thinner, fainter, and more undulating or discontinuous VE-cadherin (Fig. 2D and S4C–E), analogous to what has been described *in vivo.*[31]

Network architecture was quantified using a custom MATLAB workflow applied to day 5 confocal z-stacks (Fig. 3A and S5). This pipeline was adapted from the 3D morphometric workflow described by Song *et al.* and extended here to independently segment and quantify spatially adjacent blood and lymphatic beds, generating 3D renderings (Fig. 3B) from which volumetric coverage, vessel surface area per volume, vessel density, median vessel diameter, and median vessel segment length (node-to-node centerline distance between branching points) were extracted on a per-device basis (Fig. 3B–F).

To assess whether engineered network architecture fell within physiological ranges, we compared BEC and LEC networks at day 5. LEC vessels formed significantly wider lumens than BEC vessels (BEC: 25.80 ± 0.52 μm; LEC: 35.17 ± 1.15 μm) (Fig. 3C). The median *in vitro* vessel diameters for both networks fall within the ranges reported for human dermal blood (approximately 5–70 μm) and lymphatic (approximately 10–150 μm) microvessels (Fig. 3C). Vessel segment length (between branching points) was modestly but significantly greater in BEC networks than in LEC networks (BEC: 47.91 ± 2.18 μm; LEC: 43.86 ± 1.89 μm) (Fig. 3D). LEC networks exhibited greater vessel surface area per tissue volume, whereas BEC networks displayed higher vessel density (vessels per mm^3), mirroring human dermal tissue where blood capillary density exceeds lymphatic density but lymphatic vessels provide larger luminal surfaces for fluid uptake[32–38] (Fig. 3E and F). These data demonstrate that the device produces spatially

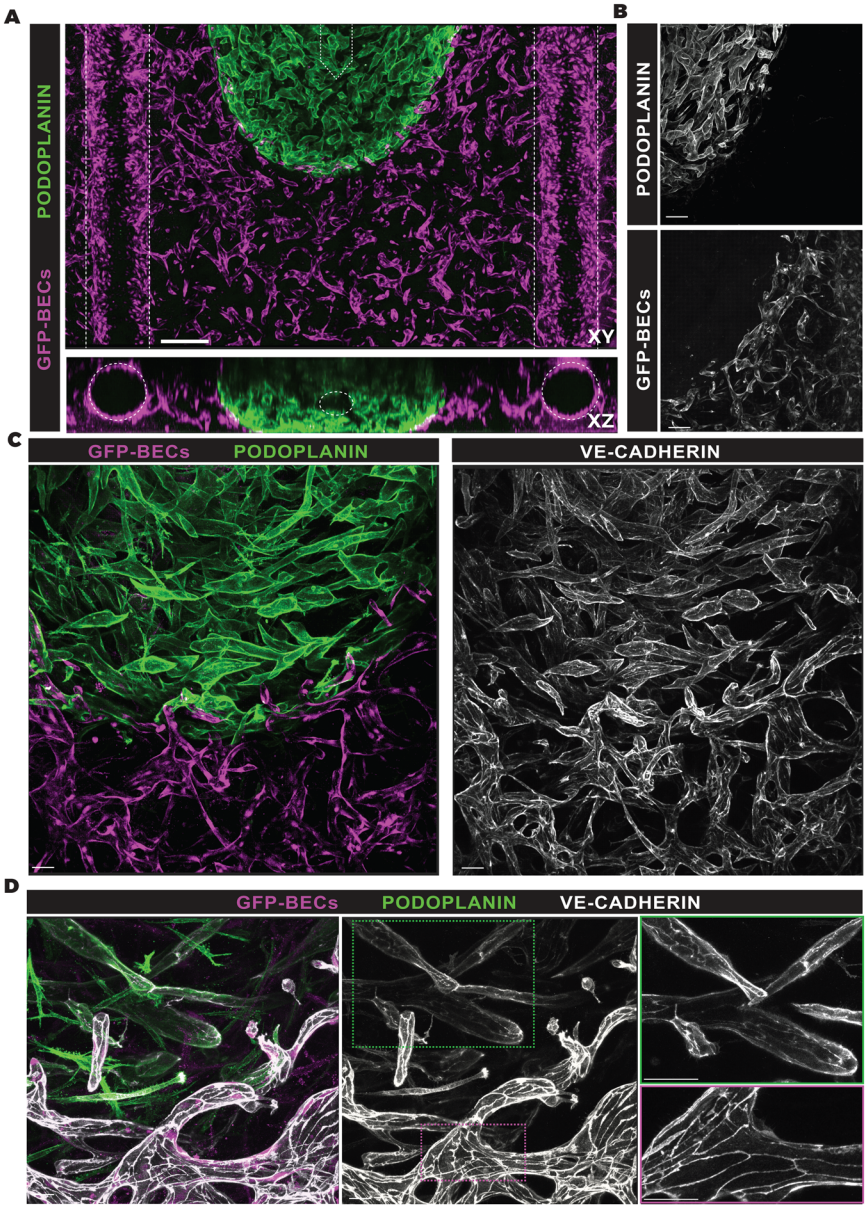

Fig. 2 Blood and lymphatic network spatial separation, adherens junction composition, and vessel morphology across scales. (A) Confocal imaging demonstrates spatial segregation of 3D BEC (GFP+, magenta) and LEC (podoplanin+, green) networks after 5 days of co-culture. White lines indicate the LEC and BEC parent channels in both top-down (*XY*) and cross-section (*XZ*) views (white circles). Scale bar: 300 μm. (B) Zoomed callout from (A) highlighting the spatial separation of both networks at the microvascular interface. Scale bar: 100 μm. (C) Confocal imaging of BEC and LEC network separation, morphology, and adherens junctions labeled by VE-cadherin (white). Scale bar: 50 μm. (D) High-resolution confocal images of the microvascular interface. Zoomed-in callouts highlight the morphology and adherens junction structure of LEC (top, green box) and BEC (bottom, pink box) microvessels near the interface. Scale bar: 100 μm in full-field images and 50 μm in zoomed callouts.

segregated, identity-stable blood and lymphatic networks with physiologically distinct morphometric signatures.

Dual-tracer perfusion demonstrates intact, independently perfusable blood and lymphatic networks

To directly examine fluidic independence between blood and lymphatic compartments, we sought to fill both vascular beds with tracers from their respective reservoirs. This is straightforward for the blood compartment, whose network connectivity mimics the physiologic direction of flow from larger vessels into capillaries with inlets and outlets; however, filling is inherently more challenging for the engineered lymphatic bed, which is blind-ended and requires retrograde infilling from the lymphatic reservoir, recognizing the limitation that it represents a transient, non-physiologic loading configuration and will not fill all dead ends equally well (Fig. S6A).

As an initial test of compartment-specific perfusion, each network was first filled individually, as shown by wide-field

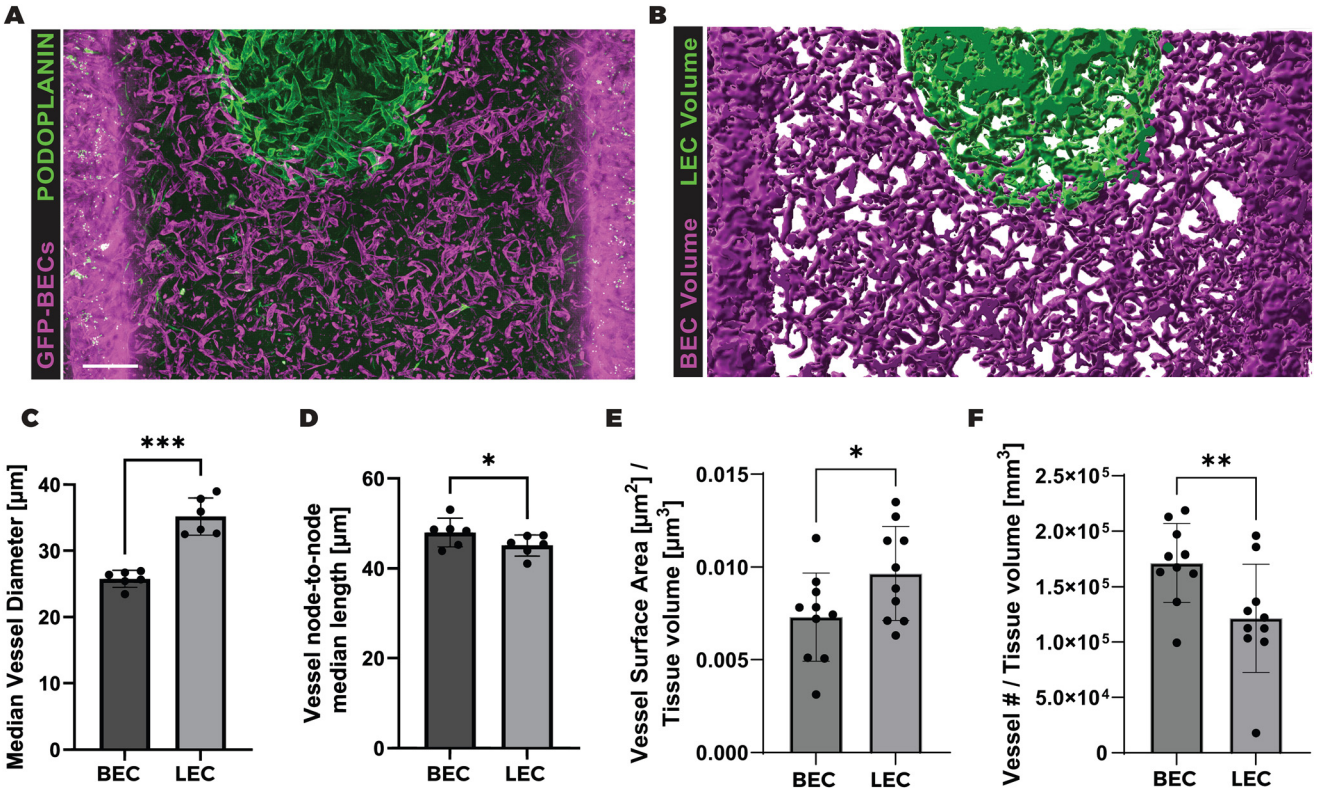

Fig. 3 Morphometric characterization of engineered blood and lymphatic microvascular networks. (A) Confocal maximum intensity projection of a representative day 5 device showing GFP-BECs (magenta) and LEC networks (podoplanin+, green). Scale bar: 300 μm. (B) Volume rendering of the segmented LEC (green) and BEC (magenta) networks from the same device. (C) Quantification of microvessel diameter for BEC and LEC networks at Day 5. Statistical comparisons were performed on device-level medians (BEC *vs.* LEC) using a paired two-tailed *t*-test (n = 6 devices from N = 3 independent experiments). (D) Quantification of vessel segment length (centerline distance between branching nodes) for BEC and LEC networks at day 5. Statistical comparisons were performed on device-level medians (BEC *vs.* LEC) using a paired two-tailed *t*-test (n = 6 devices from N = 3 independent experiments). (E) Quantification of vessel surface area per tissue volume ($\mu m^2\ \mu m^{-3}$) for Day 5 BEC and LEC networks. Bars show mean ± SD; dots represent individual devices (n = 10 devices from N = 4 independent experiments; paired two-tailed *t*-test). (F) Quantification of vessel density (vessel number per mm^3 of tissue) for day 5 BEC and LEC networks. For all morphometric comparisons, device-level metrics were first tested for normality (Shapiro–Wilk and Kolmogorov–Smirnov for diameter and length; Shapiro–Wilk, Kolmogorov–Smirnov, D'Agostino–Pearson, and Anderson–Darling for surface area and density), and normally distributed data were compared using paired two-tailed *t*-tests. Bars show mean ± SD; dots represent individual devices (n = 10 devices from N = 4 independent experiments; paired two-tailed *t*-test). $^*P < 0.05$, $^{**}P < 0.01$, $^{***}P < 0.001$.

fluorescence imaging of single-compartment tracer filling that demonstrated whole-network perfusion and overall architecture for both vascular beds (Fig. S6B). To observe the blood-lymphatic vasculature interface as higher resolution, simultaneous dual-compartment perfusion was then performed by first introducing 2000 kDa dextran into the lymphatic reservoir to retrograde infill the lymphatic vasculature, and then subsequently perfusing fluorescent beads from the blood reservoirs. At the blood–lymphatic microvascular interface, beads remained confined to blood vessels and dextran remained confined to lymphatic vessels, indicating distinct, non-anastomosed flow paths despite immediate spatial proximity (Fig. 4B). Because even 2000 kDa dextran will eventually diffuse, we also examined the networks by using different beads to fill each compartment and then visualizing the vascular interface by confocal imaging (Fig. 4C and S6C). These images demonstrated that beads traversed each network up to the blood–lymphatic interface without detectable mixing and revealed multiple blind-ended lymphatic microvessels with beads accumulating at their tips (Fig. 4C and S6C).

Because filling and visualizing lymphatic connectivity and blind-ended structures is particularly challenging in dual-network devices, we further generated single-network devices to isolate each vascular bed for additional analysis (Fig. S7). In BEC-only devices, fluorescent beads filled the GFP-positive blood microvasculature throughout the network, as expected for a connected, perfusable bed (Fig. S7A). In LEC-only devices, fluorescent beads also clearly perfused the lectin-positive lymphatic network, and high-resolution imaging at the gel interface enabled unambiguous visualization of blind-ended lymphatic microvessels with beads accumulating at their termini in positions corresponding to the normal BEC–LEC interface (Fig. S7B and C).

Together, these studies demonstrated that compartment-specific beads and dextran consistently filled their

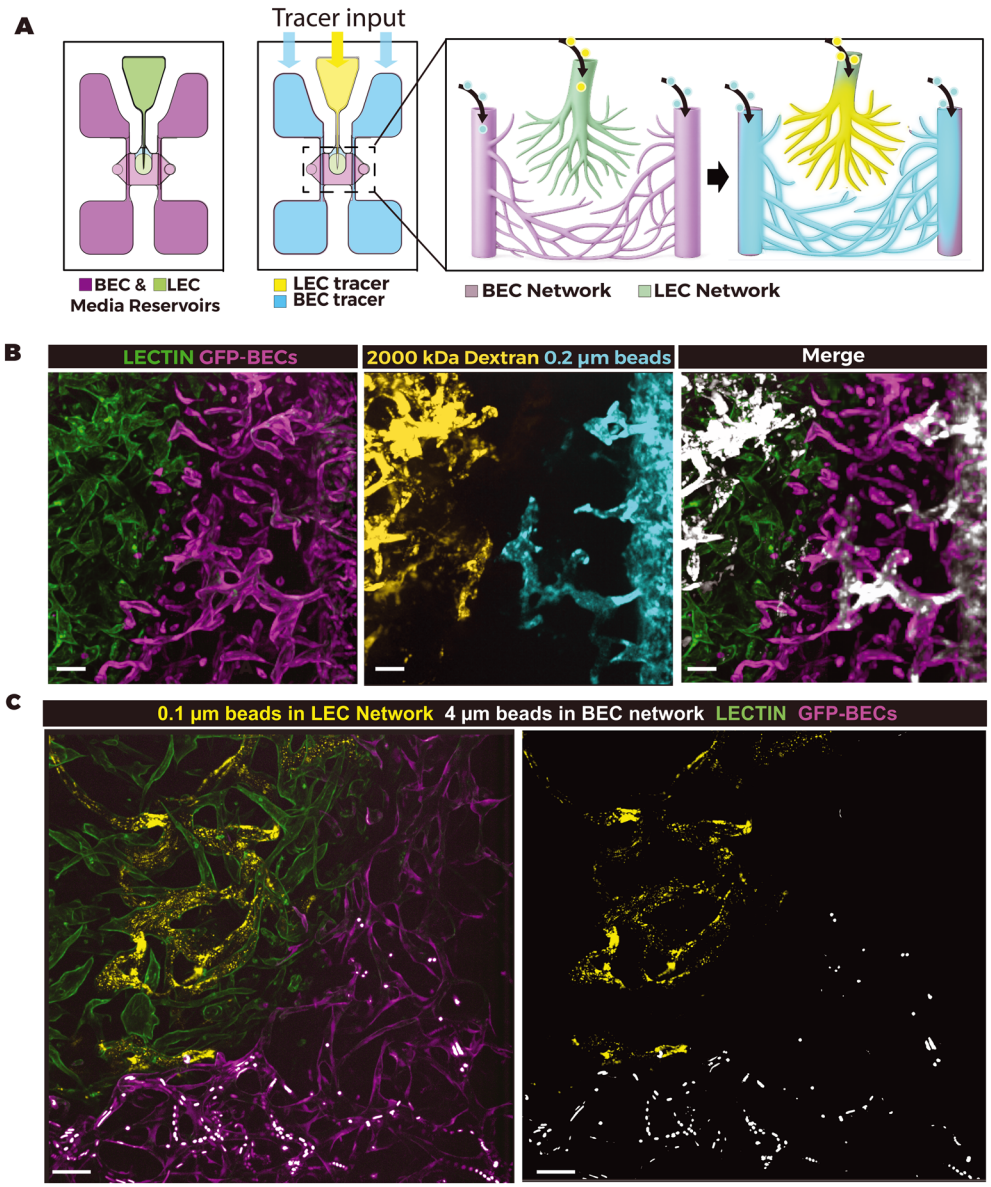

Fig. 4 Independent perfusion of blood and lymphatic vascular networks. (A) Schematic of the dye perfusion assay. Dyes were introduced into the respective parent channels to assess network connectivity and segregation. Yellow arrow indicates tracer added to the lymphatic media reservoir; cyan arrows indicate tracer added to the blood media reservoirs. (B) Live confocal imaging at the BEC–LEC microvascular interface in a 3D device where both networks are perfused simultaneously with distinct fluorescent tracers (LECs with 2000 kDa dextran in yellow, BECs with 0.2 μm beads in cyan) to demonstrate independent perfusion. BECs are shown in magenta (GFP+, lectin+), LECs in green (lectin+, GFP–). Scale bar: 150 μm. (C) Live high-resolution confocal imaging at the BEC–LEC microvascular interface in a 3D device where both networks are perfused simultaneously with distinct fluorescent beads (LECs with 0.1 μm beads in yellow, BECs with 4 μm beads in white) to demonstrate independent perfusion. BECs are shown in magenta (GFP+, lectin+), LECs in green (lectin+, GFP–), 0.1 μm beads within the LEC network in yellow, and 4 μm beads within the BEC network in white. The left panel shows all four channels, while the right panel shows only the bead channels; beads are observed throughout both networks without crossing the BEC–LEC interface. Scale bars: 80 μm.

intended networks without detectable cross-filling into the opposing compartment, and high-resolution imaging at the blood–lymphatic microvascular interface did not reveal obvious hybrid vessels or spontaneous cross lymphatic-blood vascular anastomoses (Fig. 3B–D and S6). These findings therefore established that the blood and lymphatic vasculature appeared to form distinct, fluidically independent compartments.

Flow characterization by particle tracking velocimetry

To quantify fluid flow within the engineered networks, we performed particle tracking velocimetry using compartment-specific fluorescent beads and TrackMate-based trajectory analysis (Fig. S8). In the BEC network, spatial velocity maps and bead trajectories demonstrated continuous flow paths throughout the microvascular bed, with mean bead velocities

on the order of 10^2 μm/s and peak values approaching 10^3 μm s^{-1} under maximum hydrostatic gradients used in this study, resulting in estimated wall shear stresses spanning roughly 0.1–3 dyn cm^{-2} across physiologic vessel diameters (25–200 μm) (Fig. S8C–E). In the LEC region, PTV at the outlet yielded a cumulative volumetric outflow of approximately 0.10 μL min^{-1} through a 250 × 700 μm cross-section, resulting in a bulk wall shear stress of ~0.016 dyn cm^{-2} that is further reduced when distributed across the branching lymphatic network, indicating that LEC microvessels experience substantially lower flows under these conditions (Fig. S8F–H). Together with compartment-specific bead perfusion, these measurements provide quantitative bounds on the shear landscape and further support fluidic independence of the blood and lymphatic networks used for subsequent drainage and T cell trafficking assays.

Quantitative drainage assay establishes size-selective blood-to-lymphatic transport in engineered microvascular networks

To determine whether the platform could support quantitative analysis of blood-to-lymphatic drainage, a bulk cross-network transport assay was implemented using epifluorescence imaging of the lymphatic region (Fig. 5A). Fluorescent tracers spanning a range of molecular weights and transport modes were introduced into the blood media reservoirs under a low hydrostatic pressure differential of approximately 9.6 Pa (0.07 mmHg), chosen to approximate post-capillary and interstitium-to-lymphatic pressure gradients that drive fluid and solute exchange *in vivo*,[39,40] and tracer accumulation within a predefined LEC region of interest was quantified over 3 h (Fig. 5A and S10A, C and D). The panel included 10 kDa dextran as a freely diffusing macromolecular solute, 70 kDa dextran as a commonly used surrogate for albumin-scale plasma proteins and lymph-transported biomolecules[41] 2000 kDa dextran as an extremely large macromolecular tracer used to probe barrier integrity and retention of lipoprotein-scale species,[42] and Bodipy FL C16,[43] a fluorescent long-chain fatty acid analog that reports on fatty acid uptake and transport.

Representative epifluorescent images of the lymphatic compartment illustrated time-dependent accumulation for permeant tracers (Fig. 5B). Normalized lymphatic fluorescence over 3 h revealed a clear hierarchy in transport

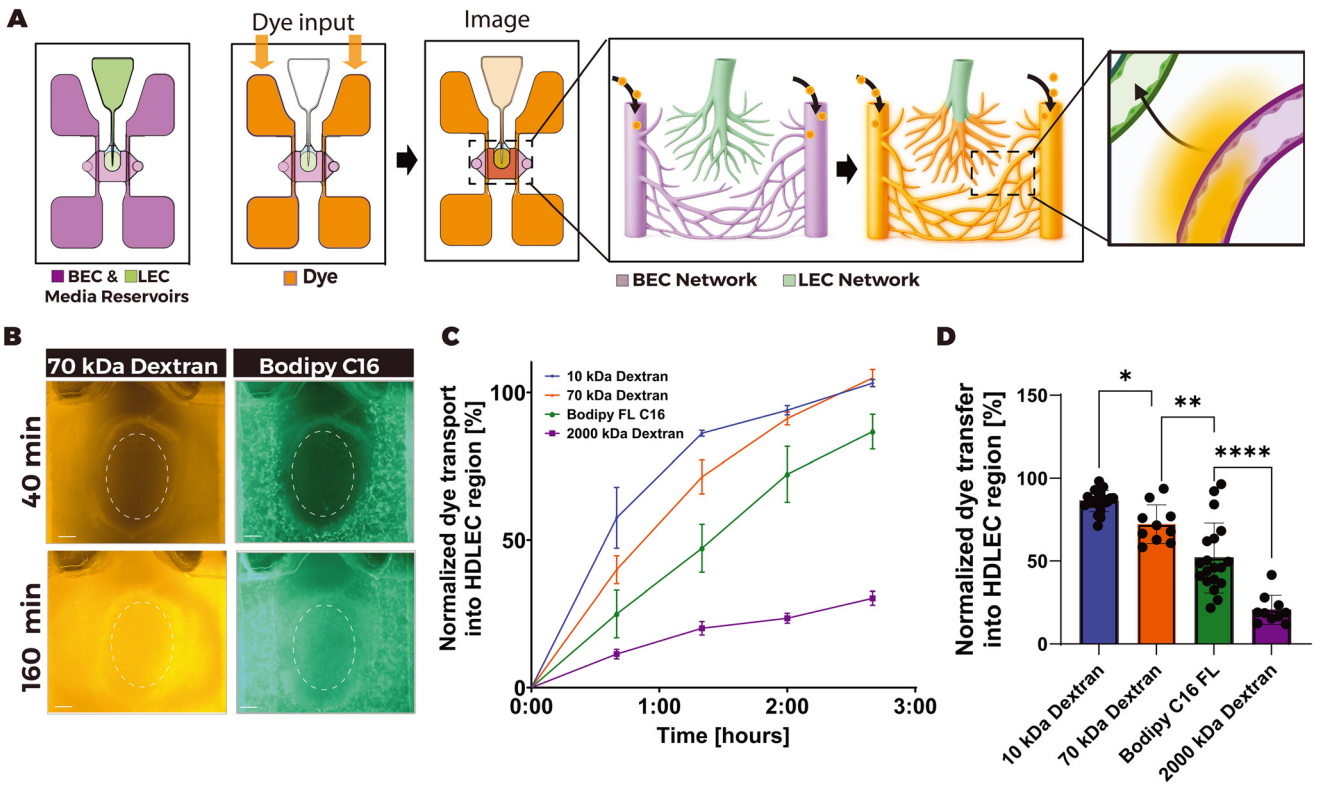

Fig. 5 Size-dependent solute transport across the blood–lymphatic interstitial interface. (A) Schematic of the cross-network transport assay. Fluorescent tracers (10, 70, or 2000 kDa dextran; or Bodipy FL C16) were introduced into the blood media reservoirs (orange arrows) under hydrostatic pressure, perfusing the blood network and transporting across the interstitium into the lymphatic network. (B) Representative fluorescence images of the lymphatic region at 40 min and 160 min after addition of 70 kDa dextran (top) or Bodipy FL C16 (bottom), illustrating time-dependent accumulation of tracer within the lymphatic compartment. (C) Normalized tracer accumulation in the lymphatic region over 3 hours. Data points represent the mean ± SD of N = 3 independent experiments (n = 10–20 total devices per dye). Scale bar: 300 μm. (D) Quantification of normalized dye transport into the lymphatic region at t = 80 min. Each dot represents an individual device from N = 3 independent experiments. Device-level values were confirmed to be normally distributed by Shapiro–Wilk testing, and groups were compared using Brown–Forsythe and Welch ANOVA with Dunnett's T3 multiple comparisons (****$P < 0.0001$).

(Fig. 5C). 10 kDa dextran accumulated fastest and reached the highest levels, 70 kDa dextran showed slightly slower but still substantial accumulation, Bodipy FL C16 accumulated to lower levels than 70 kDa dextran, and 2000 kDa dextran remained markedly lower than all other tracers throughout the assay. At t = 80 min, normalized transfer into the lymphatic region followed the ordering 10 kDa > 70 kDa > Bodipy FL C16 > 2000 kDa dextran, with overall differences across dyes highly significant ($P < 0.0001$, Brown–Forsythe and Welch ANOVA with Dunnett's T3 multiple comparisons) (Fig. 5D). Notably, 2000 kDa dextran showed minimal accumulation in the lymphatic region at all timepoints, consistent with its use in vascular studies as a high-molecular weight, largely non-permeant tracer that is retained by intact endothelial barriers, indicating that under these conditions the engineered blood–lymphatic interface effectively restricts passage of very large macromolecules.

To quantify device failure rates and exclude compromised chips from drainage analysis, we leveraged the 2000 kDa dextran channel as an in-assay barrier-integrity readout: devices were classified as failures and not used for further experimentation and analysis if a leak between blood and lymphatic compartments was identified, as detected by blood-compartment-infused dye immediately appearing in the lymphatic compartment (*i.e.*, at the first post-filling imaging time point) (Fig. S9). Using this immediate QC criterion across three independent drainage experiments, more than 80% of 2000 kDa dextran-loaded devices passed the leakage test and were retained for analysis. Failed devices showed technical issues such as gel delamination, leakage between tape layers, or casting needle intrusion into the opposing compartment rather than spontaneous cell-induced cross-network anastomosis (Fig. S9).

High-magnification confocal imaging confirmed that the bulk epifluorescent signal reflects true cross-network transport: in a representative device, 70 kDa dextran was observed within GFP-BEC blood vessels, exiting the vessel wall, traversing the acellular interstitium, and entering lectin-positive LEC lymphatic vessels at the interface (Fig. S10B), validating the underlying cross-network transport pathway. To assess whether this flow is primarily convective or diffusive in our system, recognizing that is a combination of both, we assessed the initial kinetics and spatial pattern of solute escape from blood microvessels, we performed early-phase time-lapse imaging of 70 kDa dextran and analyzed fluorescence along a line ROI extending from the blood vessel lumen into the surrounding fibrin matrix (Fig. S11A and B). Raw and vessel-normalized line profiles over the first 40 minutes showed that dextran signal remained highest within the vessel lumen at all time points, with a sharp drop in intensity at the vessel-to-matrix interface and a graded decay through the perivascular matrix (Fig. S11C–F). This pattern indicates that dye is initially retained by the endothelial barrier and then exits uniformly along the vessel wall into the surrounding gel, after which it spreads through the matrix with a spatial profile consistent with endothelial barrier-limited leakage followed by predominantly diffusive transport under the imposed pressure head, rather than rapid bulk convective filling of the gel. This analysis is also consistent with the prior convective flow analysis (Fig. S8).

Reconstitution of T cell trafficking from blood to lymphatic vasculature demonstrates platform capability for immune cell studies.

To test whether the platform could capture physiologically relevant leukocyte egress, a 4 h trafficking assay was established in which primary human $CD4^+$ and $CD8^+$ T cells were introduced *via* the blood media reservoirs after pretreatment of devices with vehicle, SDF-1α, or TNF-α (Fig. 5A). T cells were isolated from healthy donor blood by negative selection and used either as naïve cells or after activation with CD3/CD28 Dynabeads for 7 days prior to the experiment. To confirm the activation state of the T cells used in these assays, we performed flow cytometry phenotyping of post–thaw and 7-day CD3/CD28-stimulated populations (Fig. S12). The stimulated cohort showed a shift predominantly from central and effector memory to effector phenotypes indicating a shift to more cytokine production, migration, and cytotoxic function (Fig. S12A and B). The minimal change to CD69 and 41-BB is consistent with the T cells being neither recently activated (<24 hours) nor reaching late-stage activation, respectively, while significant upregulation of CD25 confirmed a mid-stage activation state. Steady expression of the adhesion integrin LFA-1 (CD11a) illustrated the activation protocol had little impact on the ability for these T cells to migrate (Fig. S12C–F). These profiles confirm that the T cells introduced into the blood network exhibit a sustained, activated phenotype rather than a resting state.

T cells perfused through the GFP-BEC network, extravasated into the interstitium, and accumulated near or within podoplanin-positive LEC vessels at the blood–lymphatic microvascular interface; orthogonal views confirmed that many cells were located inside lymphatic lumens rather than just perivascular (Fig. 6B–D and S15). Live epifluorescent imaging during the assay showed T cells transitioning from rounded to elongated morphologies as they exited BEC vessels and migrated toward the lymphatic compartment, consistent with active transmigration and interstitial motility (Fig. S13). In a representative confocal time-lapse, we observed an activated T cell that elongated within a BEC vessel, exited the blood channel, and subsequently appeared within the LEC lumen in orthogonal YZ views, providing direct visual evidence of sequential transmigration from blood to lymphatic microvessels (Fig. S14, Movie S1). After 4 h, devices were fixed, permeabilized, stained, and imaged by confocal microscopy. Three-dimensional Imaris segmentation of blood and lymphatic surfaces, combined with detection of the labeled T cells, demonstrated T cells residing within the LEC vessel volume, and counts were normalized to lymphatic tissue volume to

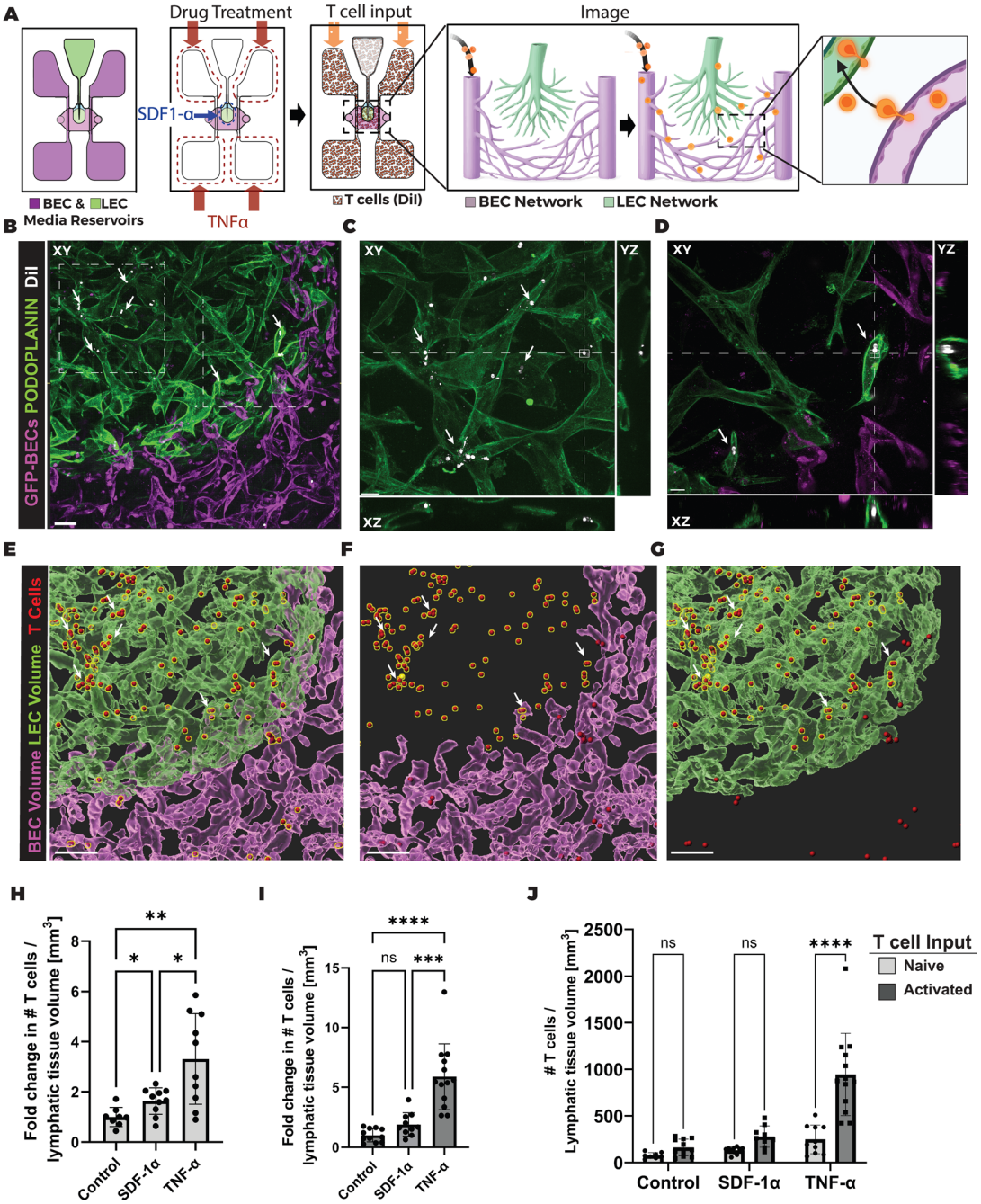

Fig. 6 Reconstitution of T cell trafficking across the blood–lymphatic interface. (A) Schematic of the T cell trafficking assay. Devices were pre-treated with TNF-α or SDF-1α, and DiL-labeled T cells (orange) were introduced into the blood media reservoirs. T cells perfused the blood network, extravasated, and migrated toward the lymphatic compartment. (B) Representative confocal image of the capillary interface after 4 hours of naïve T cell migration (control condition). Blood vessels (GFP-BEC) are magenta; lymphatic vessels (podoplanin) are green; T cells are white. White arrows indicate examples of infiltrated T cells. Dashed boxes indicate regions magnified in (C) and (D). Scale bar: 50 μm. (C and D) Magnified views with orthogonal *XZ* and *YZ* cross-sections showing T cells (white, arrows) localized within lymphatic vessels near the exit channel (C) and the capillary interface (D). Scale bar: 30 μm. (E–G) 3D segmentation and surface rendering of the vascular networks and T cells. (E) Composite rendering showing blood (magenta) and lymphatic (green) surfaces with all T cell spots (red/yellow). (F) Blood network and T cells only. (G) Lymphatic network and T cells only; T cells computationally determined to be within the lymphatic vessel volume are circled in red/yellow. Scale bar: 200 μm. (H) Fold change in naïve T cell density within the lymphatic volume for control (n = 8), SDF-1α (n = 10), and TNF-α (n = 10) conditions. Bars show mean ± SD; dots represent individual devices from N = 3 experiments. (I) Fold change in activated T cell density within the lymphatic volume for control (n = 11), SDF-1α (n = 9), and TNF-α (n = 14) conditions. Bars show mean ± SD; dots represent individual devices from N = 3 experiments. For (H) and (I), device-level values were confirmed to be normally distributed by Shapiro–Wilk testing, and groups were compared using Brown–Forsythe and Welch ANOVA with Dunnett's T3 multiple comparisons (*$P < 0.05$, **$P < 0.01$, ***$P < 0.001$, **$P < 0.0001$). (J) Comparison of naïve *versus* activated T cell trafficking into lymphatics across drug conditions. Bars show mean ± SD. Device-level values were assessed for normality using the Shapiro–Wilk test, and data were analyzed by two-way ANOVA (interaction $P < 0.0001$, drug $P < 0.0001$, activation $P < 0.0001$) followed by Šidák's multiple comparisons test (****$P < 0.0001$; ns, not significant).

yield a device-level metric of T cell density within the lymphatic network (Fig. 6E–G and S16). For all trafficking analyses, T cells were classified as residing within lymphatic vessels based on visual confirmation that their DiI signal intersected the Imaris-defined LEC surface, an operational criterion that enriches for intraluminal cells while acknowledging that some closely apposed perivascular cells may also satisfy this threshold (Fig. S16).

Using this 3D readout, we examine the effects of T cell activation and the presence of T cell chemoattractants on trafficking. Naïve T cells showed baseline trafficking into lymphatic vessels under these control conditions (fold change = 1.0 by definition). Within the naïve group, SDF-1α pretreatment increased T cell density in the lymphatic volume to 1.63-fold over control ($P < 0.05$), and TNF-α pretreatment further increased naïve trafficking to 3.31-fold over control ($P < 0.01$) (Fig. 5H). Within the activated group, SDF-1α and TNF-α increased trafficking to 1.90- and 5.89-fold over the naïve control baseline, respectively; SDF-1α showed a similar trend to the naïve condition but did not reach significance *versus* the activated control, whereas TNF-α produced a robust, statistically significant increase in activated T cell density within the lymphatic volume (Fig. 6I). When comparing absolute T cell densities between naïve and activated cells across drug conditions, there was a consistent trend toward higher numbers of activated T cells per lymphatic volume, but this difference reached statistical significance only in the presence of TNF-α (Fig. 6J). Two-way ANOVA confirmed significant main effects of drug condition and activation state, as well as a significant interaction (all $P < 0.0001$), indicating that, in this setting, the impact of activation on trafficking is most pronounced under inflammatory conditions rather than appearing as a uniform shift across all treatments. These patterns—chemokine- and TNF-α-enhanced trafficking, together with greater entry of activated T cells under inflammatory conditions—are consistent with *in vivo* observations that SDF-1α (CXCL12) and inflammatory cytokines promote T cell migration and that activation state modulates responsiveness to these cues during tissue-to-lymphatic egress.[3,44–47]

Discussion

The blood and lymphatic microvasculatures jointly regulate fluid homeostasis, solute clearance, and immune-cell trafficking,[1–3] yet most *in vitro* systems study these networks in isolation. Existing co-culture models that do generate more *in vivo* – like microvascular networks lack either physiologically relevant blood–lymphatic proximity or truly independent perfusion of both compartments,[16–25,48] limiting controlled studies of cross-network transport.[6,7] By providing physiologically relevant blood and lymphatic microvasculature in close spatial proximity while maintaining fluidic access to each compartment, the platform fills this gap and enables quantitative investigation of molecular and cellular transport at the blood–lymphatic microvascular interface.

The tape-based fabrication workflow is central to achieving this architecture. It enables the sequential casting and spatial compartmentalization required to reproducibly pattern adjacent blood and lymphatic microvascular networks in this geometry. Sequential cutting and lamination of pressure-sensitive adhesive and thermoplastic layers produce multi-layer devices with well-defined gel regions and parent channels using only benchtop tools, which also keeps material costs low and assembly straightforward.[49–53] Because the architecture exposes external media reservoirs and parent channels, the same design is compatible with future integration of recirculating pumps or controlled pressure heads to impose defined shear and interstitial flow profiles, extending the platform toward more physiologically tuned hemodynamic and lymphodynamic studies. In the present work, flow is imposed primarily through rocker-driven movement and static hydrostatic gradients, and the device's non-canonical geometry means that local flow lines and shear profiles are not fully characterized; coupling this design to computational fluid dynamics and pump-based control would help map the flow landscape and align it with physiologic ranges.[54,55]

Within this engineered geometry, morphometric analysis shows that the blood and lymphatic networks approximate key geometric features of their *in vivo* counterparts. BEC and LEC vessels form spatially segregated networks with distinct marker profiles and morphometric features, with LEC vessels displaying larger diameters and greater surface area per volume, while BEC networks exhibit higher vessel density—patterns that mirror human dermal tissue organization.[32–37] High-resolution VE-cadherin imaging further revealed continuous adherens junctions in both networks, with BEC microvessels exhibiting brighter, more linear junctions and lymphatic capillaries near the interface displaying thinner, more discontinuous, and wavier junctions at blind-ended tips, similar to what has been observed *in vivo.*[31] These distinct, physiologically scaled morphometric and junctional signatures position the platform as a controllable testbed for studying how co-culture conditions, matrix composition, or pharmacologic perturbations might differentially influence blood and lymphatic architecture in parallel; for example, future studies could probe how pro-lymphangiogenic factors, anti-angiogenic drugs, or stromal cell subsets modulate vessel diameter, density, surface area, and junctional organization in each compartment.

Establishing that these adjacent networks are fluidically independent is critical for interpreting transport assays. VE-cadherin–positive junctions along microvessels and parent channels in both compartments, combined with dual-tracer perfusion assays, show that each network can be perfused from its own reservoir without detectable cross-filling at the blood–lymphatic microvascular interface, a capability that has been challenging to achieve in previous blood–lymphatic systems. These features position the platform as a tractable,

physiologically grounded system for dissecting blood–lymphatic transport phenomena. Against this backdrop, the drainage assay demonstrates that a geometrically complex dual-network platform can still yield a simple, quantitative readout of blood-to-lymphatic transport. The ordered hierarchy of drainage (10 kDa > 70 kDa > Bodipy FL C16 ≫ 2000 kDa) mirrors *in vivo* observations that albumin-scale and smaller macromolecules traverse the blood–lymphatic interface efficiently,[41–43] whereas ultra-large dextrans are largely retained within intact vascular compartments. The minimal transfer of 2000 kDa dextran in particular is consistent with its use as a barrier-integrity probe in vascular leakage assays and provides a functional complement to the structural VE-cadherin data, indicating that the engineered interface restricts passage of very large macromolecules under near-physiological pressure gradients.

The T cell trafficking assay extends this framework from solute to cell transport and highlights how the platform's architecture can be leveraged for rare leukocyte egress events. The extended microvascular surface area and close apposition of blood and lymphatic networks increase opportunities for T cells to exit the blood, traverse the interstitium, and enter lymphatic vessels, mirroring how dense microvascular beds in tissues support immune cell egress *in vivo*. Live time-lapse imaging during the assay showed T cells transitioning from rounded to elongated morphologies as they exited blood vessels and migrated into lymphatics, consistent with active transmigration and interstitial motility.[56] Within this setting, SDF-1α and TNF-α modulate trafficking consistent with their roles as a T cell chemoattractant and key inflammatory mediator, and T cell activation further augments responsiveness under inflammatory conditions, reflecting known behaviors of effector T cells in inflamed tissues and afferent lymphatics.[44–47,57] The synergistic effect of T-cell activation and TNF-α may arise at least in part from the enhanced migratory behavior of activated T-cells coupled with the well-established ability of TNF-α to robustly increase ICAM-1 expression on blood and lymphatic endothelium,[58–60] thereby providing a conduit for enhanced trafficking. While the current trafficking experiments focus on short-term (4 hour) recruitment of resting *versus* CD3/CD28-activated $CD4^+$ and $CD8^+$ T cells from a healthy donor, future studies enabled by this platform could be extended to a broader diversity of immune cell subsets, activation states, or chronic inflammatory environments implicated in disease.

Conclusions

Here we present a tape-based microfluidic platform for studying vascular-lymphatic exchange, validating its capacity to recapitulate key physiological features through systematic characterization of morphometric architecture, size-selective drainage, and immunologically relevant T cell trafficking. The platform provides a quantitative tool for investigating transport phenomena and endothelial responses at the blood-lymphatic interface, and its modular design—compatible with pump integration, CFD-informed flow control, and expanded cellular and molecular assays—positions it for increasingly sophisticated investigations of vascular-lymphatic physiology and disease.

Materials & methods

Cell culture

Adult Human Dermal Lymphatic Microvascular Endothelial Cells ("hDMLECs" or 'LECs', Lonza, Ad-hDMVEC-Dermal, CC-2543, 99% lymphatic origin by podoplanin expression) were cultured in Microvascular Endothelial Cell Growth Medium-2 (Lonza, CC-3202, EGM-2MV) and used at passage 5. Adult Normal Human Lung Fibroblasts ("NHLFs", Lonza, CC-2512) were cultured in Fibroblast Growth Medium-2 (Lonza, FGM2, CC-3132) and used at passages 5–7. Plasma Membrane GFP-Tagged Human Dermal Microvascular Endothelial Cells ("hDMVECs" or 'BECs', Angioproteomie, cAP-0005GFP-PM) were cultured in Endothelial Cell Growth Medium-2 (Lonza, CC-3162, EGM-2) and used at passages 4–6. Primary human CD3+ and CD8+ T cells were isolated from anonymous healthy donor blood samples (Boston Children's Hospital Blood Donation Center) *via* negative selection (StemCell Technologies, RosetteSep Human T Cell Enrichment Cocktail) under an IRB-exempt protocol. For naïve T cell trafficking, cryopreserved cells were thawed 24 hours prior to use in X-VIVO 15 (Lonza, 04-418Q) with 5% human AB serum (Innovative Research, ISERAB100ML) and 100 U mL^{-1} IL-2. For activated T cell trafficking, naïve T cells were activated with Human T-Activator CD3/CD28 Dynabeads (Thermo Fisher, 11161D) at a 1 : 1 cell to bead ratio. T cells were subcultured by counting using trypan blue daily and maintaining cell concentrations between 0.5–2.0 × 10^6 cells per mL for 7 days prior to experiments.

All human cell and blood sample use was approved by the Boston University Institutional Review Board. Donor consent was obtained in accordance with institutional guidelines.

Microfluidic device design and fabrication

Tape-based microfluidic devices were assembled from cover glass, laser-cut acrylic, 3 M double-sided tapes (170 μm, 9495LE; 100 μm, 9629FL-1-60; 50 μm, 9628FL23220012), 50 μm polymer films (Universal, UNV21125), and polymer coverslips (Ibidi). Tape and polymer layers were cut using a Silhouette Cameo plotter; acrylic layers were cut by laser. Full assembly diagrams and instructions are provided in Fig. S1.

Device pre-treatment

Device interiors were functionalized with 0.01% poly-L-lysine and 1% glutaraldehyde after plasma activation, then washed overnight in DI water. Devices were dried, baked at 60 °C, and UV sterilized before seeding. Sterile 250 μm acupuncture

needles were blocked with 0.1% BSA and inserted into needle guides prior to gel casting.

Cell seeding and gel casting

Fibrin gels were prepared by dissolving 20 mg mL^{-1} fibrinogen (Sigma, F8630-5G) in DPBS (Gibco), heating to 37 °C, and sterile filtering. BECs, LECs, and NHLFs were dissociated with 0.25% Trypsin-EDTA, centrifuged, and resuspended in EGM-2MV. Two cell suspensions were prepared: (1) BECs + NHLFs, and (2) LECs + NHLFs, each at 4 : 1 ratio. Suspensions were combined with fibrinogen and thrombin (Sigma, T4648-1KU2) and sequentially cast into devices. Final gels contained 5 mg mL^{-1} fibrin, 4×10^6 BECs or LECs mL^{-1}, and 1×10^6 NHLFs mL^{-1}. Devices crosslinked for 5 minutes at 37 °C, then were hydrated with EGM-2MV and crosslinked for 15 more minutes at 37 °C before needles were removed and needle guides were sealed with vacuum grease. BEC parent channels were seeded with concentrated BECs (~10×10^6 cells per mL, 1–2 μL per channel) for 15 minutes per side at 37 °C. Devices were supplied with EGM-2MV containing 25 ng mL^{-1} VEGFA (R&D Systems, 293-VE-050), 1 ng mL^{-1} VEGFC (R&D Systems, 752-VC-025), 500 nM S1P (Cayman Chemical, 9002921), and 25 ng mL^{-1} bFGF (Thermo Fisher, PHG0261), and cultured on a rocker at 37 °C, 5% CO_2 with daily media changes for 5 days. During this culture period, devices were maintained on an orbital rocker at its lowest speed (2 rpm) with a maximum tilt angle of 30°, generating gentle oscillatory flow through the BEC parent channels, which span the 5.5 mm distance between opposing blood reservoirs. This motion produces a peak oscillatory hydrostatic head of ~27 Pa (~0.20 mmHg) across the blood parent channels but a zero time-averaged net pressure head over each rocking cycle; in contrast, the LEC compartment terminates in a dead-ended parent channel with no opposing reservoir, so rocker motion does not impose a comparable through-flow in the LEC parent channels and vessels. Note that single-network BEC-only or LEC-only devices used the same fabrication, cell suspension, casting and culturing procedures but simply omitted the alternate endothelial cell type in favor of a "blank" fibrin gel solution in that compartment to isolate each vascular bed for perfusion and imaging studies.

Immunostaining and imaging

Devices were fixed with 4% paraformaldehyde (BioLegend, 420801) in PBS for 15 minutes, followed by PBS wash and permeabilization with 0.1% Triton X-100 (Sigma, T8787) for 15 minutes. Samples were blocked overnight at 4 °C in 3% BSA (Sigma, A9647) in PBS, or 5% human A/B serum (Innovative Research, ISERAB100ML) for T cell trafficking experiments. Primary antibodies were diluted 1 : 1000 in blocking buffer and incubated overnight at 4 °C: mouse anti-human podoplanin (BioLegend, 916606), rabbit anti-human PROX1 (Abcam, ab209016), sheep anti-human CD31/PECAM-1 (R&D Systems, AF806), rabbit anti-human VE-cadherin (Cell Signaling Technology, 2500), chicken anti-GFP (Abcam, ab13970), and mouse anti-human ICAM-1/CD54 (R&D Systems, BBA3). After overnight PBS washes at 4 °C, species-appropriate secondary antibodies (1 : 1000) were incubated overnight at 4 °C: goat anti-mouse IgG Alexa Fluor Plus 647 (Invitrogen, A32728), goat anti-mouse IgG Alexa Fluor Plus 488 (Thermo Fisher, A32723), goat anti-chicken IgY DyLight 488 (Abcam, ab96947), donkey anti-sheep IgG Alexa Fluor 647 (Invitrogen, A-21448), and goat anti-rabbit IgG Alexa Fluor Plus 555 (Invitrogen, A32732). Nuclear and cytoskeletal counterstaining used DAPI (BioLegend, 422801), Alexa Fluor Plus 647 Phalloidin (Thermo Fisher, A30107), UEA I DyLight 649 (Vector Laboratories, DL-1068-1), and DiI (Invitrogen, V22885), all at 1 : 1000 dilution. Imaging was performed using a Leica SP8 laser scanning confocal microscope for network architecture and trafficking assays, a Nikon Ti2-E spinning disk confocal microscope (Andor Dragonfly 505) for live perfusion, or a Nikon TE200 epifluorescence microscope for drainage assays. Imaging settings were kept constant within each experimental cohort.

Vessel network architecture quantification

Devices were fixed and stained at days 1, 3, and 5 using primary antibodies against podoplanin (BioLegend, 916606) and GFP (Abcam, ab13970), followed by appropriate secondary antibodies. Confocal images were acquired with a 10×/0.30 NA water immersion objective using tiled z-stacks. Vascular network properties were quantified using custom MATLAB scripts (adapted from Song 2020) as previously described.[30] See Supplementary Fig. S5 for processing pipeline.

Independent dual-network perfusion

Day 5 devices were used to validate independent perfusability, connectivity, and compartmental independence of the blood and lymphatic networks. For lymphatic visualization, UEA I DyLight 649 (Vector Laboratories, DL-1068-1; 1 : 1000) was added to the lymphatic reservoir and incubated for 1–2 h at 37 °C before perfusion. Independent perfusion assays were performed under static hydrostatic pressure heads by loading reservoirs with defined volumes as described below, and live imaging was performed either on a widefield epifluorescence microscope or on a Nikon Ti2-E inverted microscope with an Andor Dragonfly 505 spinning disk confocal system maintained at 37 °C and 5% CO_2.

For LEC-only perfusion in dual-network or LEC-only devices, 40 μL of tracer solution (*e.g.*, 2000 kDa tetramethylrhodamine dextran, Thermo Fisher, D7139, or size-specific fluorescent beads such as 0.1–4 μm polystyrene tracers) was added to the single lymphatic reservoir and 10 μL of dye-free medium was added to each of the four BEC reservoirs, driving retrograde filling of the blind-ended LEC bed to visualize lymphatic connectivity and blind-ended termini. For BEC-only perfusion in dual-network or BEC-only devices, fluorescent beads (typically 0.2 μm, 405 nm; Thermo

Fisher, F13083; 1 : 1000, or 4 μm beads as indicated) were introduced into the blood reservoirs and driven through the BEC network using a brief "priming" hydrostatic configuration: all four BEC reservoirs were initially filled to 40 μL while the LEC reservoir was set to 10 μL, after which 20 μL was transferred from each of the two right BEC reservoirs to the two left BEC reservoirs (yielding 60 μL in the left and 20 μL in the right reservoirs) to push beads across the BEC parent channels and microvascular bed.

For dual-network perfusion assays in dual-network devices, the LEC compartment was first filled using the LEC-only protocol (40 μL tracer in the LEC reservoir, 10 μL in each BEC reservoir) and allowed to fill for approximately 10 min until the lymphatic network was fully loaded. The LEC reservoir was then maintained at 40 μL while compartment-specific fluorescent beads were introduced into the BEC reservoirs and the same 60/20 μL priming configuration was applied across left *versus* right BEC reservoirs to drive bead flow through the GFP^+/$lectin^+$ BEC network in parallel with tracer-filled GFP^-/$lectin^-$ lymphatic vessels. In some experiments, single-network devices containing only BECs or only LECs were perfused using the corresponding BEC-only or LEC-only loading schemes to isolate each vascular bed and facilitate high-resolution imaging of network connectivity and lymphatic blind-ended structures.

Flow characterization within networks by particle tracking velocimetry (PTV)

To quantify the fluid environment within the BEC and LEC networks, devices were perfused with size-specific fluorescent polystyrene tracers (FluoSpheres™, Thermo Fisher Scientific, Waltham, MA, USA). The BEC network was perfused with 4 μm diameter green-fluorescent beads, while the LEC network was selectively perfused with 0.1 μm diameter red-fluorescent beads. This dual-size tracer approach was employed to ensure compartment-specific tracking and to verify the lack of physical coupling between the two independent networks.

PTV experiments were performed under the 60/20 μL priming hydrostatic gradient, mirroring the maximal flow conditions experienced during BEC network filling, and were therefore intended to provide upper-bound estimates of velocities and shear. Starting from a baseline configuration in which all four BEC reservoirs were at 40 μL and the LEC reservoir at 10 μL, this transient gradient was imposed by transferring 20 μL of medium from the two downstream BEC reservoirs to the two upstream BEC reservoirs, resulting in upstream reservoirs at 60 μL and downstream reservoirs at 20 μL while maintaining the LEC reservoir at 10 μL, thereby driving flow through the BEC microvascular compartment as well as toward the lymphatic outlet.

Imaging was performed using an Andor Dragonfly (Andor Technology, Belfast, UK) spinning disk confocal microscope mounted on a Nikon Ti2 inverted microscope body (Nikon Corporation, Tokyo, Japan). Environmental stability was maintained using a full-enclosure Okolab incubation system (Okolab S.r.l., Pozzuoli, Italy), maintained at 37 °C and 5% CO2. To achieve the high temporal resolution required for fast-moving tracers in the BEC network, the system was operated in Live Mode with exposure times optimized between 2.5 and 10 ms. Video was acquired *via* OBS Studio (OBS Project, USA) screen capture of the live feed, ensuring a consistent frame rate of 30 fps without software-induced dropped frames.

The resulting video files were imported into FIJI (ImageJ) and calibrated for spatial and temporal scales. Bead trajectories were analyzed using the TrackMate plugin. A Laplacian of Gaussian (LoG) detector was utilized for spot identification, with estimated blob diameters set to 6 μm (BEC) and 10 μm (LEC). Tracks were generated using a Simple LAP Tracker with a maximum linking distance of 15 μm and 30 μm gap-closing to maintain the fidelity of instantaneous velocity measurements.

Instantaneous velocity was calculated as $v = \Delta d/\Delta t$. Spatial velocity maps were generated by plotting the coordinates of each detected displacement, color-coded by speed, to visualize localized flow gradients.

The cumulative volumetric flow rate (Q) was estimated at the primary supply channel (cross-section: 250 × 700 um) using the equation $Q = v_{mean} \times A$, where v_{mean} is the mean particle velocity and A is the cross-sectional area. Theoretical wall shear stress (τ) was calculated in dyn cm^{-2} assuming a Newtonian fluid with a dynamic viscosity (μ) of 0.001 Pa s at 37 °C. For the multi-scale branching architecture, shear stress was estimated across a range of vessel diameters (D) using the Hagen-Poiseuille derivation: $\tau = 8\mu v/D$.

For the branching LEC network, the cumulative flow exiting the region was treated as a bulk estimate; local shear stresses within individual distal branches were acknowledged to be further partitioned by the network architecture, resulting in a negligible mechanical state (estimated at less than 0.02 dyn cm^{-2}).

Drainage assay and quantification

Day 5 devices were used for bulk drainage assays. Blood reservoirs were loaded with 10 kDa Cascade Blue dextran (Invitrogen, D1976), BODIPY FL C16 (Invitrogen, D3821), and either 70 kDa Texas Red dextran (Invitrogen, D1864) or 2000 kDa Tetramethylrhodamine dextran (Thermo Fisher, D7139). Before starting image acquisition, blood microvessels were primed by sequentially loading 40 μL of dextran-containing medium into individual BEC reservoirs on one side of the device, allowing flow to propagate across the network and partially fill the remaining reservoirs, followed by loading the remaining BEC reservoirs to 40 μL; the lymphatic reservoir was maintained at 10 μL of dye-free EGM-2MV throughout. This procedure established flow through the BEC network while keeping reservoir volumes near their target values. To apply the physiological hydrostatic pressure conditions used for quantitative drainage measurements (9.6 Pa net differential from BEC to LEC), all four BEC reservoirs were at

40 μL and the lymphatic reservoir at 10 μL at the start of the assay. Devices were incubated statically for 3 hours at 37 °C. Fluorescence images of the lymphatic region were captured every 30 minutes for 2.5 hours using a 4× air objective on a Nikon TE200 epifluorescence microscope. Mean fluorescence intensity in the lymphatic region was quantified using ImageJ (NIH), baseline-subtracted using paired control devices, and normalized to mean intensity of dye-loaded blood parent channels at final timepoint. See Fig. S7 for quantification details.

Live microscopy early-phase analysis of 70 kDa dextran leakage from blood microvessels

A permeability assay was performed using Texas Red-conjugated 70 kDa dextran on a Nikon Ti Eclipse epifluorescence microscope equipped with an environmental chamber (37 °C, 5% CO_2). Epifluorescence imaging was performed in GFP (488 nm) and Cy3 (Texas Red, 550 nm) channels using a Plan Apo 10× objective. Time-lapse images were acquired every 3 minutes for 40 minutes starting at $t = 0$ to capture initial permeability kinetics. Before starting image acquisition, blood microvessels were primed by sequentially loading 40 μL of dextran-containing medium into individual BEC reservoirs on one side of the device, allowing flow to propagate across the network and partially fill the remaining reservoirs, followed by loading the remaining BEC reservoirs to 40 μL; the lymphatic reservoir was maintained at 10 μL of dye-free EGM-2MV throughout. This procedure established flow through the BEC network while keeping reservoir volumes near their target values. To apply the physiological hydrostatic pressure conditions used for quantitative permeability measurements (9.6 Pa net differential from BEC to LEC), all four BEC reservoirs were at 40 μL and the lymphatic reservoir at 10 μL at the start of imaging. Z-Stacks (~20 slices, 10 μm z-step) were captured for each region of interest at every time point. Videos, images, and line-profile measurements were generated in ImageJ/Fiji, where a straight-line ROI was drawn through a GFP-BEC vessel and into the adjacent fibrin matrix to quantify dextran intensity along the vessel-to-gel axis over time (Fig. S11).

Flow cytometry for T cell phenotyping

Post-thaw/resting and 7-day CD3/CD28-activated T cells were analyzed by flow cytometry on an Attune NxT (Thermo Fisher Scientific). Cells were suspended in 150 μL fresh culture media, and at least 10 000 live events were collected per sample (n = 6 biological replicates per condition). Live lymphocytes were gated by forward and side scatter, then single cells by FSC-A *versus* FSC-H and further subdivided into $CD4^+$ and $CD8^+$ subsets. Naïve/memory status was assessed using CD45RA and CCR7 (CD45RA BV421, BioLegend 304130; CCR7 APC, Thermo Fisher 17-1979-42); activation status using CD69, CD25, and 4-1BB (CD69 APC, BD Biosciences RD21710F; CD25 BV605, BioLegend 302632; 4-1BB PE-Cy7, BioLegend 309818); and adhesion integrin expression using LFA-1 (CD11a FITC, Thermo Fisher 11-0111-82). CD4 and CD8 subsets were identified using CD4 PE (R&D Systems FAB3791P) and CD8 FITC (Thermo Fisher 11-0086-42). Compensation was performed with UltraComp eBeads (Thermo Fisher Scientific), and data were analyzed in FlowJo.

T cell trafficking assay and quantification

Day 5 devices were used for T cell trafficking studies. T cells were labeled with DiI (Invitrogen, V22885) per manufacturer protocol. For inflammatory conditions, devices were pre-treated for 4 hours with 10 ng mL^{-1} TNF-α (PeproTech, 300-01A) in EGM-2MV across all reservoirs. For chemotactic conditions, 50 μL of 100 ng mL^{-1} SDF-1α (PeproTech, AF-300-28A) was added to the lymphatic gel region reservoir 10 minutes before T cell loading. Media was removed from all reservoirs, and 2×10^6 labeled T cells in dye-free EGM-2MV were first introduced into individual BEC reservoirs by sequentially loading 40 μL on one side of the device and then the opposite side to initiate flow through the BEC network while maintaining near-target reservoir volumes; the lymphatic reservoir was maintained at 10 μL during loading. At the start of the trafficking assay, all four BEC reservoirs were adjusted to 40 μL and the lymphatic reservoir to 10 μL, establishing a low, physiological hydrostatic pressure differential (9.6 Pa) from BEC to LEC. Devices were incubated statically for 4 hours at 37 °C, then fixed, permeabilized, and stained. Imaging was performed on a Leica SP8 confocal microscope (10× objective). T cells within lymphatic networks were quantified in Imaris using spot detection following LEC network segmentation, and counts were normalized to lymphatic tissue volume. For all trafficking analyses, T cells were classified as residing within lymphatic vessels based on visual confirmation that their DiI signal intersected the Imaris-defined LEC surface (Fig. S16). For the live imaging series shown in Fig. S14 and Movie S1, devices were imaged on a Nikon Ti2-E spinning disk confocal microscope (Andor Dragonfly 505) approximately 2 hours into the trafficking assay, acquiring time-lapse z-stacks every 10 minutes. For these live experiments, LECs were identified as lectin-positive, GFP-negative vessels and BECs as lectin-positive, GFP-positive vessels.

Data analysis and statistics

Analyses were performed using GraphPad Prism (version 10.2.2), MATLAB (MathWorks 2020a), and Imaris. The statistical test, number of independent biological replicates (n), and number of independent experiments (N) are reported in the figure legends. No data points were excluded unless a clear technical failure was identified (for example, device leakage due to gel delamination).

For network architecture analysis, the image-processing pipeline identified all vessel segments within each device and returned, for each segment, the centerline length (node-to-node distance between branching points) and corresponding

local vessel diameter, along with whole-network summary metrics of vessel surface area per tissue volume and vessel density. All statistical comparisons were performed at the device level to avoid pseudo-replication, treating each device as a single experimental unit. Specifically, for diameter and segment length, the median value per device was used, and for surface area per volume and vessel density, the single network-level value per device was used. These device-level summary values were assessed for normality using the Shapiro–Wilk test and, when normally distributed, were compared between blood and lymphatic networks using paired two-tailed t-tests, leveraging the fact that each blood–lymphatic network pair was generated within the same device.

For multi-group comparisons (for example, dye transport and T cell trafficking assays), device-level values were first tested for normality using the Shapiro–Wilk test. Datasets that met normality assumptions were analyzed by Brown–Forsythe and Welch one-way ANOVA with Dunnett's T3 post-hoc test to account for unequal variances and unequal sample sizes, or by two-way ANOVA with appropriate multiple comparisons corrections, as implemented in GraphPad Prism. The specific tests used for each analysis are indicated in the corresponding figure legends.

Figure generation

Schematics and graphical abstracts were created using BioRender, llustrae, and Adobe Illustrator.

Author contributions

Conceptualization: D. G.-S., T. C., C. S. C. Methodology: D. G.-S., T. C., A. C. I. v. S., S. C. A., E. D., C. S. C. Software: D. G.-S. Validation: D. G.-S., T. C., A. C. I. v. S., K. B., T. R., S. C. A. Formal analysis: D. G.-S., T. C., S. C. A., K. B., T. R. Investigation: D. G.-S., T. C., K. B., A. C. I. v. S., S. C. A., E. D. Resources: C. S. C., W. W. W. Data curation: D. G.-S., T. C., K. B., S. C. A., E. D., T. R. Writing – original draft: D. G.-S., T. C., S. C. A. Writing – review & editing: D. G.-S., T. C., S. C. A., E. D., K. B., T. R., J. E., C. S. C. Visualization: D. G.-S., T. C., S. C. A. Supervision: J. E., W. W. W., C. S. C. Project administration: J. E., C. S. C. Funding acquisition: C. S. C.

Conflicts of interest

There are no conflicts to declare.

Data availability

The data supporting this article have been included as part of the supplementary information (SI). Data for this article, including code, and metadata are available at the OSF registry at: https://osf.io/ckyu6/overview?view_only=bc9e59eded204e05b3a824afbf5f199f.

Supplementary information: detailed device assembly protocols are available in supplementary information. See DOI: https://doi.org/10.1039/d5lc01171j.

Acknowledgements

This work was supported by the National Institutes of Health (HL175072; EB033821) and the Wellcome Leap HOPE Program. D. G.-S. received support from the Boston University Clinical and Translational Science Institute (CTSI) TL1 fellowship NIH/NCATS UL1TR001430 and the Boston University Kilachand Multicellular Design Program Kilachand Fellowship.

References

1 T. V. Petrova and G. Y. Koh, *Science*, 2020, **369**(6500), eaax4063.
2 H. Wiig and M. A. Swartz, *Physiol. Rev.*, 2012, **92**, 1005–1060.
3 G. Oliver, J. Kipnis, G. J. Randolph and N. L. Harvey, *Cell*, 2020, **182**(2), 270–296.
4 J. D. Shields, M. Borsetti, H. Rigby, S. J. Harper, P. S. Mortimer, J. R. Levick, A. Orlando and D. O. Bates, *Br. J. Cancer*, 2004, **90**, 693–700.
5 M. W. Dewhirst and T. W. Secomb, *Nat. Rev. Cancer*, 2017, **17**, 738–750.
6 A. R. Henderson, H. Choi and E. Lee, *Micromachines*, 2020, **11**, 147.
7 A. Selahi and A. Jain, *Microcirculation*, 2023, **30**(2–3), e12793.
8 H. H. G. Song, R. T. Rumma, C. K. Ozaki, E. R. Edelman and C. S. Chen, *Cell Stem Cell*, 2018, **22**, 340–354.
9 S. Kim, H. Lee, M. Chung and N. L. Jeon, *Lab Chip*, 2013, **13**, 1489–1500.
10 M. L. Moya, Y. H. Hsu, A. P. Lee, C. W. H. Christopher and S. C. George, *Tissue Eng., Part C*, 2013, **19**, 730–737.
11 I. K. Zervantonakis, S. K. Hughes-Alford, J. L. Charest, J. S. Condeelis, F. B. Gertler and R. D. Kamm, *Proc. Natl. Acad. Sci. U. S. A.*, 2012, **109**, 13515–13520.
12 S. Kim, M. Chung and N. L. Jeon, *Biomaterials*, 2016, **78**, 115–128.
13 E. Lee, S.-L. Chan, Y. Lee, W. J. Polacheck, S. Kwak, A. Wen, D.-H. T. Nguyen, M. L. Kutys, S. Alimperti, A. M. Kolarzyk, T. J. Kwak, J. Eyckmans, D. R. Bielenberg, H. Chen and C. S. Chen, *Proc. Natl. Acad. Sci. U. S. A.*, 2023, **120**, e2308941120.
14 C. P. Ng, C. L. E. Helm and M. A. Swartz, *Microvasc. Res.*, 2004, **68**, 258–264.
15 A. M. Kolarzyk, G. Wong and E. Lee, *Cold Spring Harbor Perspect. Med.*, 2022, **12**(9), a041169.
16 M. Sato, N. Sasaki, M. Ato, S. Hirakawa, K. Sato and K. Sato, *PLoS One*, 2015, **10**, e0137301.
17 H.-Y. Cho, J.-H. Choi, K.-J. Kim, M. Shin and J.-W. Choi, *Front. Bioeng. Biotechnol.*, 2020, **8**, 611802.
18 X. Cao, R. Ashfaq, F. Cheng, S. Maharjan, J. Li, G. Ying, S. Hassan, H. Xiao, K. Yue and Y. S. Zhang, *Adv. Funct. Mater.*, 2019, **29**, 100–106.

19 L. Knezevic, M. Schaupper, S. Mühleder, K. Schimek, T. Hasenberg, U. Marx, E. Priglinger, H. Redl and W. Holnthoner, *Front. Bioeng. Biotechnol.*, 2017, **5**, 260650.
20 A. Nishiguchi, M. Matsusaki, Y. Asano, H. Shimoda and M. Akashi, *Biomaterials*, 2014, **35**, 4739–4748.
21 D. Marino, J. Luginbühl, S. Scola, M. Meuli and E. Reichmann, *Sci. Transl. Med.*, 2014, **6**(221), 221ra14.
22 M. Matsusaki, K. Fujimoto, Y. Shirakata, S. Hirakawa, K. Hashimoto and M. Akashi, *J. Biomed. Mater. Res., Part A*, 2015, **103**, 3386–3396.
23 S. Landau, A. Newman, S. Edri, I. Michael, S. Ben-Shaul, Y. Shandalov, T. Ben-Arye, P. Kaur, M. H. Zheng and S. Levenberg, *Proc. Natl. Acad. Sci. U. S. A.*, 2021, **118**, 1–12.
24 M. Chung, J. Ahn, K. Son, S. Kim and N. L. Jeon, *Adv. Healthcare Mater.*, 2017, **6**, 1–7.
25 T. Osaki, J. C. Serrano and R. D. Kamm, *Regener. Eng. Transl. Med.*, 2018, **4**, 120–132.
26 J. Bourland, J. Fradette and F. A. Auger, *Sci. Rep.*, 2018, **8**, 1–13.
27 M. Kang, W. Park, S. Na, S. M. Paik, H. Lee, J. W. Park, H. Y. Kim and N. L. Jeon, *Small*, 2015, **11**, 2789–2797.
28 M. Jang, P. Neuzil, T. Volk, A. Manz and A. Kleber, *Biomicrofluidics*, 2015, **9**, 1–12.
29 U. N. Lee, J. H. Day, A. J. Haack, R. C. Bretherton, W. Lu, C. A. Deforest, A. B. Theberge and E. Berthier, *Lab Chip*, 2020, **20**, 525–536.
30 H.-H. G. Song, A. Lammers, S. Sundaram, L. Rubio, A. X. Chen, L. Li, J. Eyckmans, S. N. Bhatia and C. S. Chen, *Adv. Funct. Mater.*, 2020, **30**, 2003777.
31 P. Baluk, J. Fuxe, H. Hashizume, T. Romano, E. Lashnits, S. Butz, D. Vestweber, M. Corada, C. Molendini, E. Dejana and D. M. McDonald, *J. Exp. Med.*, 2007, **204**, 2349–2362.
32 T. Hoshino, Y. Cheng, M. Ninomiya, M. Katsuyama, T. Yamashita, C. Katagiri, R. K. Wang and Y. Hara, *Quant. Imaging Med. Surg.*, 2024, **14**, 6238–6249.
33 M. Skobe and M. Detmar, *J. Invest. Dermatol. Symp. Proc.*, 2000, **5**, 14–19.
34 A. M. Talkington, R. B. Davis, N. C. Datto, E. R. Goodwin, L. A. Miller and K. M. Caron, *Front. Cardiovasc. Med.*, 2022, **9**, 840305.
35 J. Cracowski and M. Roustit, *Compr. Physiol.*, 2020, **10**, 1105–1154.
36 M. Fischer, U. K. Franzeck, I. Herrig, U. Costanzo, S. Wen, M. Schiesser, U. Hoffmann and A. Bollinger, *Am. J. Physiol.*, 1996, **270**, H358–H363.
37 S. Rui, Z. Cao, Y. Wang and L. Liu, *Sci. Rep.*, 2025, **15**, 1–12.
38 J. W. Breslin, Y. Yang, J. P. Scallan, R. S. Sweat, S. P. Adderley and W. L. Murfee, *Compr. Physiol.*, 2018, **9**, 207–299.
39 M. Sawdon and E. Kirkman, *Anaesthesiol. Intensivmed.*, 2023, **24**, 291–297.
40 V. H. Huxley and J. Scallan, *J. Physiol.*, 2011, **589**, 2935–2943.
41 W. J. Polacheck, M. L. Kutys, J. B. Tefft and C. S. Chen, *Microfabricated blood vessels for modeling the vascular transport barrier*, Springer US, 2019, vol. 14.
42 M. Bartosova, D. Ridinger, I. Marinovic, J. Heigwer, C. Zhang, E. Levai, J. H. Westhoff, F. Schaefer, S. Terjung, G. Hildenbrand, D. Krunic, F. Bestvater, M. Hausmann, C. P. Schmitt and S. G. Zarogiannis, *Int. J. Mol. Sci.*, 2021, **22**, 1–15.
43 J. B. Dixon, S. Raghunathan and M. A. Swartz, *Biotechnol. Bioeng.*, 2009, **103**, 1224–1235.
44 S. A. Luther, A. Bidgol, D. C. Hargreaves, A. Schmidt, Y. Xu, J. Paniyadi, M. Matloubian and J. G. Cyster, *J. Immunol.*, 2002, **169**, 424–433.
45 L. A. Johnson, R. Prevo, S. Clasper and D. G. Jackson, *J. Biol. Chem.*, 2007, **282**, 33671–33680.
46 S. Okabe, S. Fukuda, Y. J. Kim, M. Niki, L. M. Pelus, K. Ohyashiki, P. P. Pandolfi and H. E. Broxmeyer, *Blood*, 2005, **105**, 474–480.
47 M. C. Blades, A. Manzo, F. Ingegnoli, P. R. Taylor, G. S. Panayi, H. Irjala, S. Jalkanen, D. O. Haskard, M. Perretti and C. Pitzalis, *J. Immunol.*, 2002, **168**, 4308–4317.
48 L. Gibot, T. Galbraith, J. Bourland, A. Rogic, M. Skobe and F. A. Auger, *Nat. Protoc.*, 2017, **12**, 1077–1088.
49 T. Ching, A. C. I. van Steen, D. Gray-Scherr, J. L. Teo, A. Vasan, J. Jeon, J. Shah, A. Patel, A. E. Stoddard, J. L. Bays, J. Eyckmans and C. S. Chen, *Lab Chip*, 2025, **25**, 1474–1488.
50 Z. Wu, G. Ma, A. Wang, G. Zhang, S. Zhong, K. Zhao, Q. Wang, Y. Li and K. P. Chen, *J. Microelectromech. Syst.*, 2025, **34**, 594–602.
51 S. R. A. Kratz, C. Eilenberger, P. Schuller, B. Bachmann, S. Spitz, P. Ertl and M. Rothbauer, *Sci. Rep.*, 2019, **9**, 1–12.
52 S. Smith, M. Sypabekova and S. Kim, *Biosensors*, 2024, **14**(5), 249.
53 L. E. Stallcop, Y. R. Álvarez-García, A. M. Reyes-Ramos, K. P. Ramos-Cruz, M. M. Morgan, Y. Shi, L. Li, D. J. Beebe, M. Domenech and J. W. Warrick, *Lab Chip*, 2018, **18**, 451–462.
54 N. K. Rajeeva Pandian, A. Farrell, E. Davis, S. Sundaram, A. C. I. van Steen, J. L. C. Teo, J. Eyckmans and C. S. Chen, *Bioeng. Transl. Med.*, 2025, 1–13.
55 J. W. Song, S. P. Cavnar, A. C. Walker, K. E. Luker, M. Gupta, Y. C. Tung, G. D. Luker and S. Takayama, *PLoS One*, 2009, **4**(6), e5756.
56 M. C. Hunter, A. Teijeira and C. Halin, *Front. Immunol.*, 2016, **7**, 613.
57 G. J. Randolph, S. Ivanov, B. H. Zinselmeyer and J. P. Scallan, *Annu. Rev. Immunol.*, 2017, **35**, 31–52.
58 W. E. Cromer, S. D. Zawieja, B. Tharakan, E. W. Childs, M. K. Newell and D. C. Zawieja, *Angiogenesis*, 2014, **17**, 395–406.
59 Y. Sawa, Y. Sugimoto, T. Ueki, H. Ishikawa, A. Sato, T. Nagato and S. Yoshida, *J. Histochem. Cytochem.*, 2007, **55**, 721–733.
60 J. S. Pober, *Arthritis Res.*, 2002, **4**(Suppl 3), S109–S116.

